Composites Part B 79 (2015) 649–659

Contents lists available at ScienceDirect

Composites Part B

journal homepage: www.elsevier.com/locate/compositesb

Preparation of reduced graphene oxide-$NiFe_2O_4$ nanocomposites for the electrocatalytic oxidation of hydrazine

Md. Elias Uddin [a], Nam Hoon Kim [a], Tapas Kuila [b], Seung Hee Lee [a], David Hui [c], Joong Hee Lee [a, d, *]

[a] Advanced Materials Institute of BIN Technology (BK21 Plus Global), Department of BIN Convergence Technology, Chonbuk National University, Jeonju, Jeonbuk 561-756, Republic of Korea
[b] Surface Engineering & Tribology Division, CSIR-Central Mechanical Engineering Research Institute, Council of Scientific & Industrial Research (CSIR), Mahatma Gandhi Avenue, Durgapur 713209, India
[c] Department of Mechanical Engineering, University of New Orleans, New Orleans, LA 70148, USA
[d] Carbon Composite Research Center & Department of Polymer & Nano Science and Technology, Chonbuk National University, Jeonju, Jeonbuk 561-756, Republic of Korea

ARTICLE INFO

Article history:
Received 11 April 2015
Accepted 14 May 2015
Available online 23 May 2015

Keywords:
A. Nano-structures
D. Thermal analysis
B. Chemical properties
D. Electron microscopy

ABSTRACT

A reduced graphene oxide (RGO)-$NiFe_2O_4$ nanocomposite was synthesized by a simple one step hydrothermal approach and its application in the electrocatalytic oxidation of hydrazine was demonstrated. The as-synthesized nanocomposite was characterized by X-ray diffraction, Fourier transform infrared spectroscopy, UV–visible spectroscopy, X-ray photoelectron spectroscopy (XPS), Raman spectroscopy, Thermogravimetric analysis, Field emission-scanning electron microscopy (FE-SEM), and Transmission electron microscopy (TEM). The FE-SEM and TEM image analyses revealed that the $NiFe_2O_4$ nanoparticles were uniformly distributed on the RGO sheets with a diameter and length of ~10 and ~100 nm, respectively. The XPS analysis confirmed the ionic states of Ni and Fe to be Ni^{3+} and Ni^{2+}, and Fe^{2+} and Fe^{3+}, respectively. Further, the electrochemical activity of the RGO-$NiFe_2O_4$ nanocomposite was investigated by studying the oxidation of hydrazine. The RGO-$NiFe_2O_4$ modified glassy carbon electrode (GCE) showed an outstanding electrocatalytic activity towards the oxidation of hydrazine as compared to the $NiFe_2O_4$ and RGO modified electrodes. The enhanced electrocatalytic activity is due to the synergistic effect between RGO and $NiFe_2O_4$. Using amperometry, the lowest detection limit of 200 nM was achieved with the RGO-$NiFe_2O_4$ modified GCE. Therefore, the RGO-$NiFe_2O_4$ modified GCE can be used for the electrochemical oxidation of hydrazine.

1. Introduction

Hydrazine is the simplest diamine, a highly reactive base, and a reducing agent. Hydrazine and its derivatives are broadly utilized in applications including fuel cells, catalysts, blowing agents, corrosion inhibitors, antioxidants, pharmaceutical intermediates, pesticides, plant-growth regulators, and dyes in addition to their use as starting materials in the synthesis of some insecticides and photography materials [1–3]. Moreover, hydrazine is a high energy molecule which can be used as a fuel in explosives and rocket propulsion systems [4]. It is also used in hydrazine/air direct-liquid fuel cells are used due to their advanced equilibrium potential, non-explosive and less toxic in dilute solution [5]. However, despite of its wide range of applications, pure hydrazine is highly toxic and harmful to human life. In order to detect low concentrations of hydrazine and to resolve the associated environmental issues, a suitable cost-effective electrocatalyst must be developed [6,7]. Recently, the determination of hydrazine has been reported using various modified electrodes such as gold nanoparticles supported on a TiO_2 nanotube [8], titanium-supported Ag electrode [9], metal electrodes [10], carbon nanotubes/Ni–Fe alloys [11], carbon-supported metalloporphyrins [12], iridium [13], palladium-polyaniline nanocomposites [14], nickel–palladium nanoparticles [15], and Ni–Co alloy modified electrodes [16]. In addition, the electrochemical determination of hydrazine was also reported in *in situ* grown ceria nanoparticles

* Corresponding author. Advanced Materials Institute of BIN Technology (BK21 Plus Global), Department of BIN Convergence Technology, Chonbuk National University, Jeonju, Jeonbuk 561-756, Republic of Korea. Tel.: +82 63 270 2342; fax: +82 63 270 2341.
E-mail address: jhl@chonbuk.ac.kr (J.H. Lee).

http://dx.doi.org/10.1016/j.compositesb.2015.05.029
1359-8368/

over a reduced graphene oxide (RGO) modified electrode by Srivastava et al. [17].

It is well known that mixed transition metal oxide nanoparticles are suitable electrode materials due to their fascinating structural, electronic, and magnetic activities, which improve their catalytic properties [18]. Controlling the size and morphology of mixed metal oxide nanoparticles (NPs) will improve the performance of the catalyst [19]. The strong van der Waals' force of attraction and the high surface energy of metal oxide NPs cause the NPs to aggregate in the absence of capping agents. Therefore, it is necessary to use a capping ligand or solid supports to minimize aggregation as well as improve the morphology and performance of the catalyst [20]. In this work, RGO was used as the solid supporting material to protect the nickel ferrite NPs from aggregation.

Nickel-ferrite is one of the most malleable and important spinel compounds due to its typical ferromagnetic properties and high electrochemical stability. The term spinel is broadly used to identify compounds with a general formula of MFe_2O_4 (M = divalent metal ion, e.g. Ni, Co, Mn, Zn, etc.). Nickel-ferrite crystallizes with an inverse spinel structure, i.e. tetrahedral sites are occupied by ferric ions and the octahedral sites are occupied by ferric and nickel ions. It is expected that $NiFe_2O_4$ could also be used as an electrocatalyst apart from its electronic and magnetic applications due to its conducting nature [21]. It has already been demonstrated that $NiFe_2O_4$ exhibits good electrochemical stability and hence, can be used as a material for hybrid supercapacitors, Li ion batteries, and electrocatalysts [22].

Graphene, the mother of all carbon nanostructures, consists of a 2D monolayer of carbon atoms patterned in a honeycomb network. Increasing attention has been paid towards graphene due to its potential applications in electronics, sensors, catalysis, and energy-storage systems [23]. It has fascinating electronic, mechanical, and thermal properties compared to any other material in the world. In addition, its large surface area and highly conducting nature of graphene make it an ideal electrode material. It has also been shown that graphene could be used for anchoring various NPs [24,25]. However, controlling the size and spatial distribution of NPs on the surface of graphene is very important. Therefore, remarkable effort has been devoted to the deposition and size control of the metal NPs on the surface of graphene [26]. Due to the synergistic effect of graphene and metal oxide NPs, the properties of composites which have potential applications in catalysis, sensor, and energy-storage devices have greatly improved [27]. In the present study, RGO-supported $NiFe_2O_4$ (RGO-$NiFe_2O_4$) nanocomposites were synthesized via a facile single step hydrothermal method. The synthesized material was characterized using various spectroscopic and microscopic techniques. A nanocomposite-modified glassy carbon electrode was prepared by a drop casting method and used for the electrochemical determination of hydrazine. In comparison to bare GCE, $NiFe_2O_4$, and RGO, the nanocomposite exhibited a higher catalytic activity. Therefore, RGO-$NiFe_2O_4$ nanocomposites could be an efficient material for the electro-oxidation and detection of hydrazine.

2. Experimental methods

2.1. Materials

Natural graphite flakes (300 mesh), nickel (II) chloride hexahydrate ($NiCl_2.6H_2O$), iron (III) chloride hexahydrate ($FeCl_3.6H_2O$), and sodium thiosulfate ($Na_2S_2O_3.5H_2O$) were purchased from Sigma–Aldrich (Germany). Sulfuric acid (H_2SO_4), hydrochloric acid (HCl), hydrogen peroxide (H_2O_2), and potassium permanganate ($KMnO_4$) was purchased from Samchun Pure Chemical Co. Ltd (Korea). All the reagents were used without further purification.

2.2. Synthesis of graphene oxide (GO)

Graphite oxide was prepared using natural graphite flakes following a modified Hummer's method [28]. In brief, about 2 g of graphite flakes was added into a round bottom flask and then, 46 mL of concentrated H_2SO_4 (95%) was poured into the flask. The flask was subsequently placed in an ice bath. Next, about 6 g of $KMnO_4$ was added slowly to the above mixture under vigorous stirring while keeping the reaction temperature below 5 °C for ~2 h. Further, the reaction was carried out at 35 °C for ~6 h in a preheated oil bath. During this reaction, the color of the mixture changed from black to light brown. To this mixture, ~92 mL of double distilled water was slowly added and vigorously stirred for another 1 h. After this, 30% H_2O_2 was added until the color of the mixture turned to a golden yellow. Subsequently, 5% HCl was also added into to the above mixture to remove the excess amount of manganese. The obtained suspension was purified through high speed centrifugation using double distilled water several times. Finally, GO was obtained after the filtration and vacuum drying treatment.

2.3. Synthesis of the RGO-$NiFe_2O_4$ nanocomposite

The RGO-$NiFe_2O_4$ nanocomposite was synthesized by a hydrothermal method. About 50 mg of GO was dispersed into 40 mL of double distilled water via ultrasonication for 30 min. Subsequently, 0.25 mg of $FeCl_3.6H_2O$ and 0.125 mg of $NiCl_2.6H_2O$ was mixed into 40 mL of double distilled water. This above mixture of metal salts was added drop-wise into the prepared solution of GO under vigorous stirring to obtain a homogeneous suspension. Consequently, 0.1 g of sodium thiosulfate ($Na_2S_2O_3.5H_2O$) was added to the above mixture and stirred for 1 h. To this mixture, a 5 M aqueous solution of NaOH was added to adjust the pH to ~11. The as-prepared mixture was transferred into a 100 mL of Teflon-lined autoclave. The reaction was carried at 150 °C for 20 h and then cooled to room temperature, naturally. The obtained black precipitate was collected and washed with double distilled water followed by ethanol. This slurry type product was further dried at 60 °C in a vacuum oven for ~72 h to obtain the final RGO-$NiFe_2O_4$ product. Following the above steps, pure RGO and $NiFe_2O_4$ were also synthesized.

3. Measurements and characterizations

3.1. Characterizations

Fourier transform infrared spectra (FT-IR) of the samples were recorded in the range of 400–4000 cm^{-1} using a Nicolet 6700 spectrometer (Thermo Scientific, USA). For the FT-IR measurements, samples were mixed with KBr and thereafter, pellets were prepared. The crystalline features and phase formation of the synthesized samples were examined by obtaining X-ray diffraction (XRD) patterns using a D/Max 2500 V/PC (Cu Ka, k = 1.5406 Å; Rigaku Corporation, Japan). The Raman spectra were recorded at room temperature using a Nanofinder 30 (Tokyo Instruments Co., Japan) over the spectral range of 100–3000 cm^{-1}. The chemical compositions and nature of the synthesized samples were probed through X-ray photoelectron spectroscopy (XPS) (KBSI Daejeon Center Axis-Nova, Kratos Analytical Ltd., UK). The optical properties and energy band gaps of the synthesized samples were examined by UV–visible spectroscopy (UVS-2100 SCINCO spectrophotometer). Thermogravimetric analysis (TGA) was carried out on a Q50 TGA (TA Instruments, USA) at a heating rate of 5 °C min^{-1} from 35 to 800 °C under a N_2 atmosphere. The surface morphology of the synthesized products was probed by field emission scanning electron microscopy (FE-SEM) JSM-6701F (JEOL, Japan). The shapes and

sizes of the synthesized samples were investigated using a high resolution transmission electron microscope (HR-TEM) and obtaining selected area electron diffraction (SAED) patterns.

3.2. Electrode preparation and electrochemical measurements

Prior to the fabrication of the electrodes, the glassy carbon electrode (GCE) was carefully polished using alumina paste (0.05 μm). The polished GCE was rinsed with acetone and water by ultrasonication and dried in a vacuum at room temperature. After that, 2.5 mg of the catalyst was dispersed in ethanol (200 μl) as the solvent and Nafion (3 wt. %) as the binder, followed by ultrasonic treatment for 30 min. The as-prepared solution (10 μl) was carefully drop casted onto the surface of GCE and further dried at 30 °C in a vacuum oven. For the controlled experiments, RGO and $NiFe_2O_4$-modified GCEs were prepared by a similar method.

The electrochemical properties of the synthesized materials were measured using a CHI660A potentiostat/galvanostat with a three-electrode system. Platinum wire and saturated Ag/AgCl (sat. KCl) were used as the counter and reference electrodes, respectively. The modified GCE (diameter of 3 mm) was used as the working electrode. All of the electrochemical measurements were carried out at room temperature using a 1 M KOH aqueous solution as the electrolyte under a nitrogen atmosphere unless otherwise specified. For the differential pulse voltammetric (DPV) measurements, a pulse width of 0.06 s, amplitude of 0.05 V, a sample period of 0.02 s, and a pulse period of 0.20 s were applied.

4. Results and discussion

4.1. XRD patterns

Fig. 1 shows the XRD patterns of the synthesized products. The XRD pattern of GO exhibits a diffraction peak at $2\theta = 11.2°$ with an interlayer spacing of 0.79 nm, corresponding to the (002) plane [29]. The XRD pattern of RGO shows a broad peak at $2\theta = 26.1°$, which is attributed to the reduction of GO into RGO [30]. Furthermore, in the case of RGO, the interlayer spacing of 3.64 A° is slightly larger than that of pristine graphite (3.40 A°). The increased d-spacing for RGO is ascribed to the presence of a small amount of oxygen containing functional groups [31]. The XRD patterns of $NiFe_2O_4$ and the RGO-$NiFe_2O_4$ composite exhibit four diffraction peaks which can be indexed to the (311), (400), (511), and (440) planes of the cubic and face centered spinel type $NiFe_2O_4$ structure (JCPDS-73-1702) [32]. In addition, a broad diffraction peak centered at $2\theta = 26°$ is also observed, which is correlated to the characteristic peak of RGO. These observations suggest that $NiFe_2O_4$ was successfully grown on the surface of the RGO sheets resulting in the formation of the RGO-$NiFe_2O_4$ nanocomposite.

4.2. FT-IR spectroscopy

FT-IR spectra of GO, RGO, $NiFe_2O_4$, and the RGO-$NiFe_2O_4$ composite are shown in Fig. 2. In the FT-IR spectrum of GO, the peaks around 3426 and 1399 cm^{-1} are ascribed to O–H stretching and deformation vibrations, respectively. The peaks around 1,730, 1,626, 1,215, 1,080, and 750 cm^{-1} are attributed to C=O stretching vibrations from carbonyl groups, C=C vibrations from the aromatic carbon, C–OH stretching vibrations, C–O vibrations from epoxy groups, and C–O vibrations from alkoxy groups, respectively [33]. However, in the FT-IR spectrum of RGO, the peak for the epoxide group vanishes whereas the hydroxyl group peak still remains although the intensity of these peaks are significantly reduced compared to GO, confirming the reduction of GO by the hydrothermal treatment. Further, in the case of $NiFe_2O_4$ and the RGO-$NiFe_2O_4$ composite, bands related to oxygen moieties are not observed. Nevertheless, absorption peaks near 1570 and 591 cm^{-1} appeared in $NiFe_2O_4$ and the RGO-$NiFe_2O_4$ composite, which are attributed to the skeletal vibration of graphene and the metal-oxygen bonds of the $NiFe_2O_4$ crystal, respectively [34].

4.3. UV–Vis spectroscopy

Fig. 3(a) shows the UV–Vis spectra of GO, RGO, and the RGO-$NiFe_2O_4$ nanocomposite. The UV–Vis spectrum of GO exhibits a broad absorption band near ~230 nm corresponding to the $\pi \rightarrow \pi^*$ transition of C=C, whereas the small band at ~300 nm is attributed to the $n \rightarrow \pi^*$ transitions of C=O, suggesting the presence of oxygen-containing functional groups in GO [35]. The UV–Vis spectrum of RGO shows an absorption band around 285 nm which can be used to monitor the reduction of GO. The UV–Vis spectrum of the $NiFe_2O_4$ NPs and RGO-$NiFe_2O_4$ nanocomposite shows an

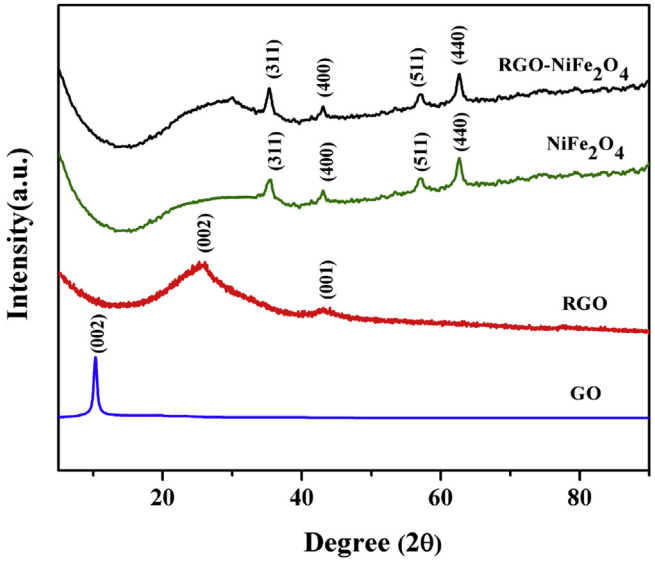

Fig. 1. XRD patterns of GO, RGO, $NiFe_2O_4$, and RGO-$NiFe_2O_4$ nanocomposite.

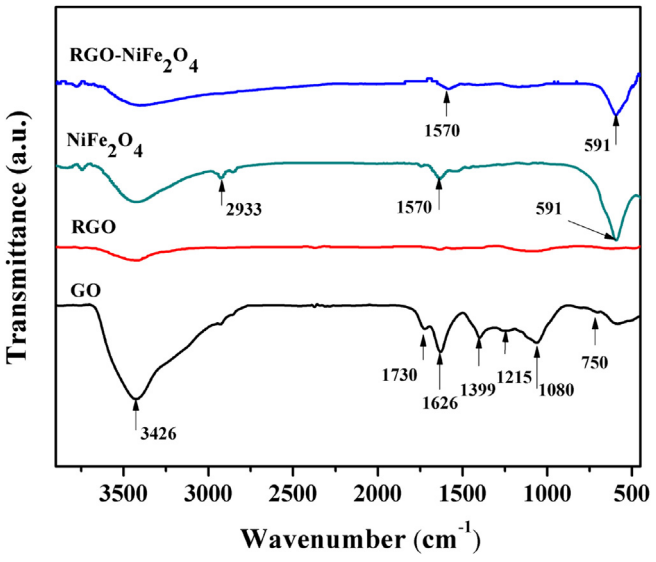

Fig. 2. FT-IR spectra of GO, RGO, $NiFe_2O_4$, and RGO-$NiFe_2O_4$ nanocomposite.

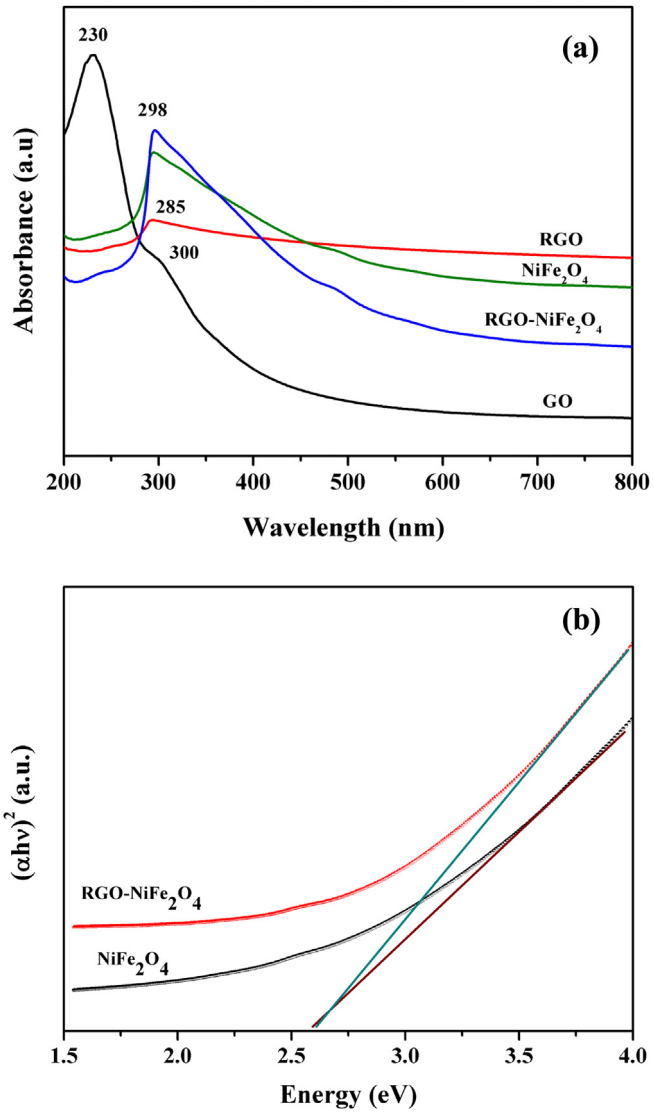

Fig. 3. (a) UV–Vis spectra of GO, RGO, $NiFe_2O_4$, and RGO-$NiFe_2O_4$ nanocomposite and (b) Tauc plots [$(\alpha h\upsilon)^2$ vs. $h\upsilon$] for $NiFe_2O_4$ and RGO-$NiFe_2O_4$ nanocomposite.

absorption band at ~298 nm. In addition, a slight variation of the UV–Vis spectrum of the RGO-$NiFe_2O_4$ nanocomposite was observed, indicating that chemical bonding between the $NiFe_2O_4$ nanoparticles and RGO form in the composite [36].

The optical band gaps in the $NiFe_2O_4$ nanoparticles and RGO-$NiFe_2O_4$ nanocomposite were determined from the Tauc plots [$(\alpha h\upsilon)^2$ vs. $h\upsilon$] shown in Fig. 3(b). The band gap energies were calculated to be 2.57 and 2.61 eV for $NiFe_2O_4$ and the RGO-$NiFe_2O_4$ nanocomposite, respectively. It is known that the band gap of semiconductor nanoparticles decreases as their size increases. The slightly higher value of the band gap of the RGO-$NiFe_2O_4$ nanocomposite compared to the bare $NiFe_2O_4$ nanoparticles is attributed to the smaller size of the $NiFe_2O_4$ particles compared to RGO-$NiFe_2O_4$ [37].

4.4. Raman spectroscopy

Raman spectroscopy is one of the most sensitive and useful techniques to characterize disordered features in sp^2 carbon materials [38]. The Raman spectra of GO, RGO, and the RGO-$NiFe_2O_4$ nanocomposite show two prominent peaks in the range of 1250–1450 cm^{-1} and 1500–1605 cm^{-1}, which correspond to the D and G bands of graphene, respectively, as shown in Fig. 4. The D band appears due to the disruption of the symmetrical hexagonal graphitic lattice as a result of internal structural defects, edge defects, and dangling bonds. The G band corresponds to the in-plane stretching motion of the symmetrical sp^2 C–C bonds [39]. In the Raman spectrum of the RGO-$NiFe_2O_4$ nanocomposite, a few additional bands in the spectral range of 300–700 cm^{-1} are also observed. These bands are characteristic of the spinel type $NiFe_2O_4$ structure. These results suggest the formation of the RGO-$NiFe_2O_4$ nanocomposite [40]. The intensity ratio of the D and G bands (I_D/I_G) can be used to investigate the degree of disorder and average size of the sp^2 domains [41]. The I_D/I_G ratio in the case of RGO is slightly higher than that of GO, suggesting a higher degree of defects in RGO compared to GO. However, in the case of the RGO-$NiFe_2O_4$ nanocomposite, the I_D/I_G ratio was significantly lower than those of GO and RGO. The above results indicate that the degree of defects in the RGO-$NiFe_2O_4$ nanocomposite was lower than those of GO and RGO [42].

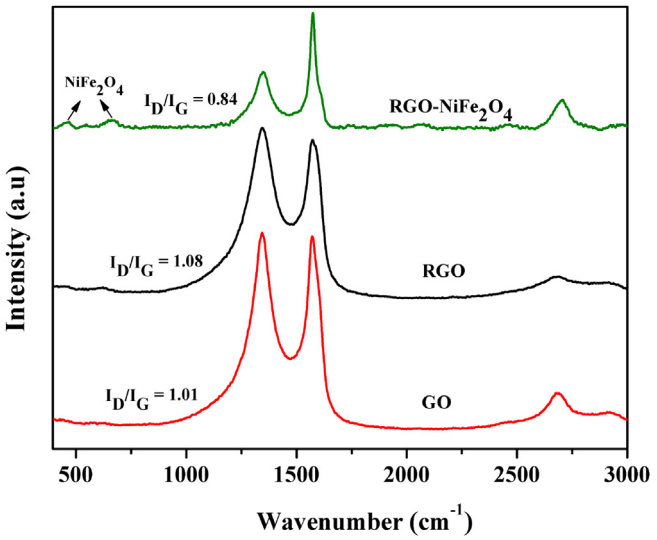

Fig. 4. Raman spectra of GO, RGO, and RGO-$NiFe_2O_4$ nanocomposite.

4.5. Thermal analysis

The thermal properties of GO, RGO, and the RGO-$NiFe_2O_4$ nanocomposite were examined by TGA and the results are shown in Fig. 5. It is known that GO is thermally unstable and weight loss starts below 100 °C due to the loss of humidity. The majority of the weight loss occurred around 200 °C due to the pyrolysis of oxygen-containing functional groups, yielding CO, CO_2, and vapor [43]. A weight loss of ~55% in GO was observed at ~700 °C, which indicates that the graphite was extensively oxidized. On the other hand, in the case of RGO, a weight loss of ~43% was observed at the same temperature. It can be seen that the RGO-$NiFe_2O_4$ nanocomposite experienced weight loss in three main steps. The weight loss below 100 °C is attributed to the evaporation of absorbed water. Gradual weight loss occurred from 100 to 290 °C which can be correlated to the removal of oxygen-containing functional groups and vapor. A significant weight loss of ~15% occurred between 590 and 700 °C. Based on the TGA results of the RGO-$NiFe_2O_4$ nanocomposite, the weight ratio of RGO to $NiFe_2O_4$ was calculated to be ~30%.

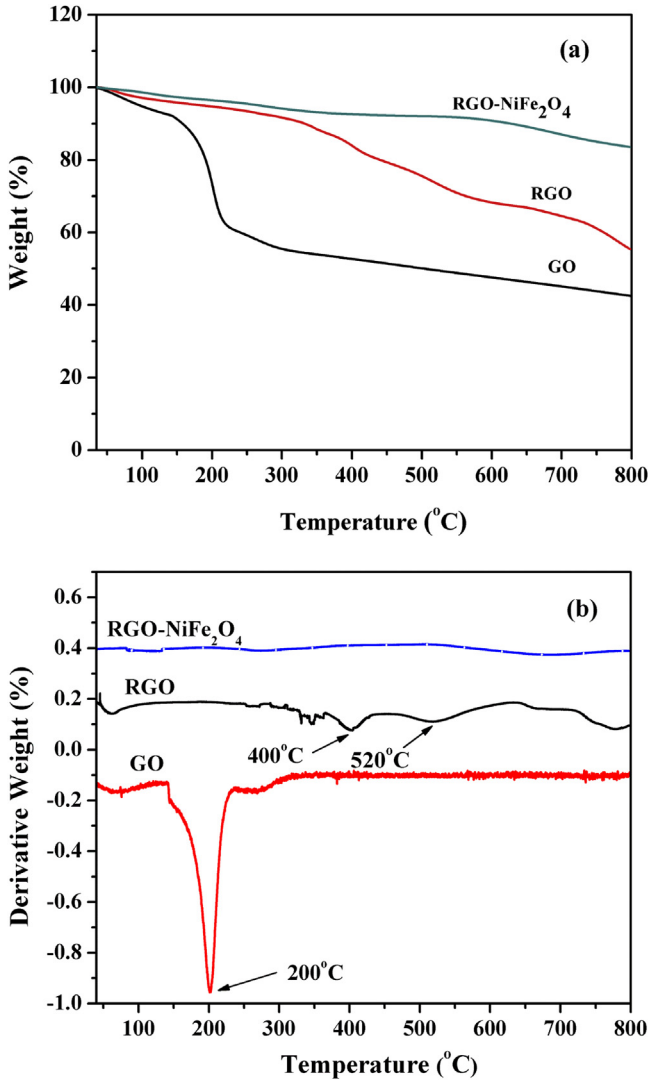

Fig. 5. (a) TGA and (b) DTA curves of GO, RGO, and RGO-$NiFe_2O_4$ nanocomposite.

4.6. FE-SEM and TEM analyses

Fig. 6(a–c) shows FE-SEM micrographs of $NiFe_2O_4$, RGO, and the RGO-$NiFe_2O_4$ nanocomposite. It can be seen that $NiFe_2O_4$ nanoparticles are homogeneously distributed over the entire region and have a spherical morphology. Further, the grain size of the $NiFe_2O_4$ nanoparticles is observed to be in the range of 20–50 nm. It can be seen that RGO possesses dry leaf-type morphology. On the other hand, the FE-SEM images of the RGO-$NiFe_2O_4$ nanocomposite clearly show that $NiFe_2O_4$ particles are densely grown on the RGO sheets with a grain size of 20–40 nm.

The TEM micrographs of the $NiFe_2O_4$ nanoparticles shown in Fig. 7(a) reveal that particles are nearly spherical in shape with a size of ~5 nm. The SAED pattern [inset of Fig. 7(a)] of the $NiFe_2O_4$ nanoparticles exhibits diffraction rings, signifying the polycrystalline nature of the $NiFe_2O_4$ nanoparticles. The HR-TEM image of $NiFe_2O_4$ nanoparticles shown in Fig. 7(b) shows grains aligned in different directions with interplanar spacings of 0.253 nm, 0.418 nm, and 0.48 nm, which are consistent with the (311), (200), and (111) planes, respectively, of the $NiFe_2O_4$ phase calculated from the XRD pattern. The TEM micrograph of RGO shows a transparent film-like structure with crumple wrinkles Fig. 7(c) and the corresponding SAED pattern shows a bright spot with six-fold symmetry

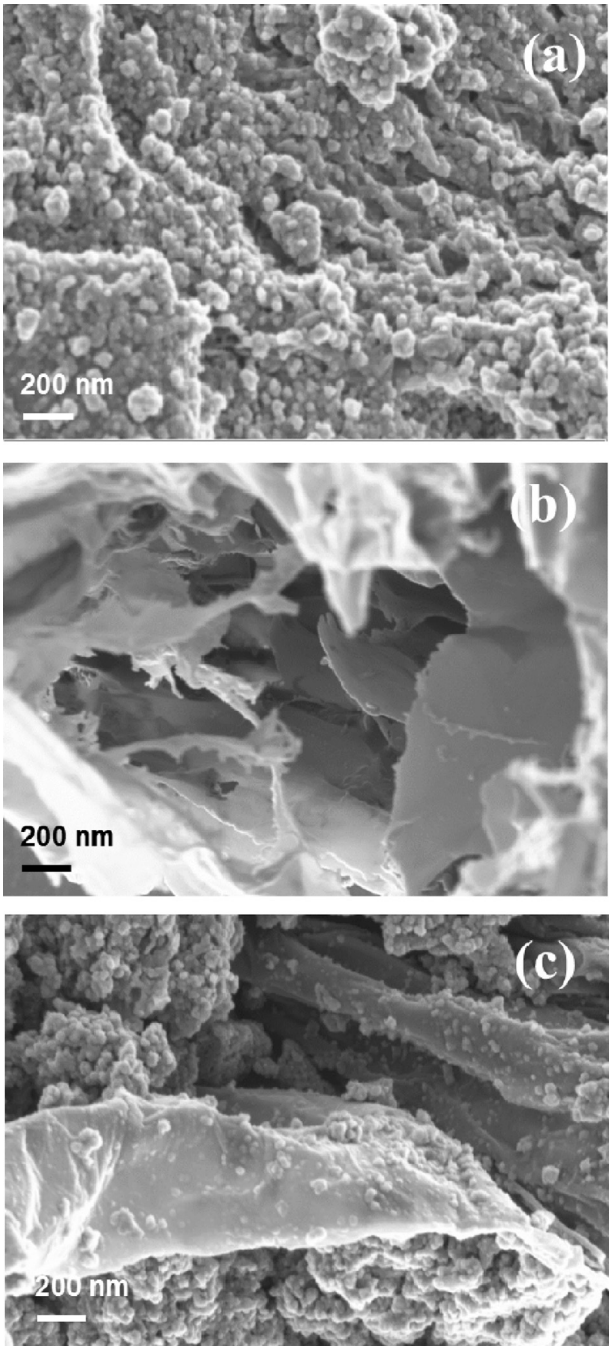

Fig. 6. FE-SEM images of (a) $NiFe_2O_4$ nanoparticles, (b) RGO, and (c) RGO-$NiFe_2O_4$ nanocomposite.

comprising the features of graphene. The HR-TEM image of an edge presented in Fig. 7(d) enables determination of the number of layers in RGO, suggesting that RGO consists of 4–5 layers [44]. Fig. 7(e and f) display TEM and HR-TEM micrographs of the RGO-$NiFe_2O_4$ nanocomposite. It can be seen that $NiFe_2O_4$ nanoparticles with sizes of ~5 nm are homogeneously distributed on the surface of RGO. The corresponding SAED pattern [inset of Fig. 7(e)] also shows diffraction rings along with a bright spot with six-fold symmetry, signifying the polycrystalline nature of the RGO-$NiFe_2O_4$ nanocomposite. Further, the HR-TEM image of the RGO-$NiFe_2O_4$ nanocomposite reveals that the $NiFe_2O_4$ nanoparticles are irregular and nearly spherically shaped where lattice fringes are clearly seen.

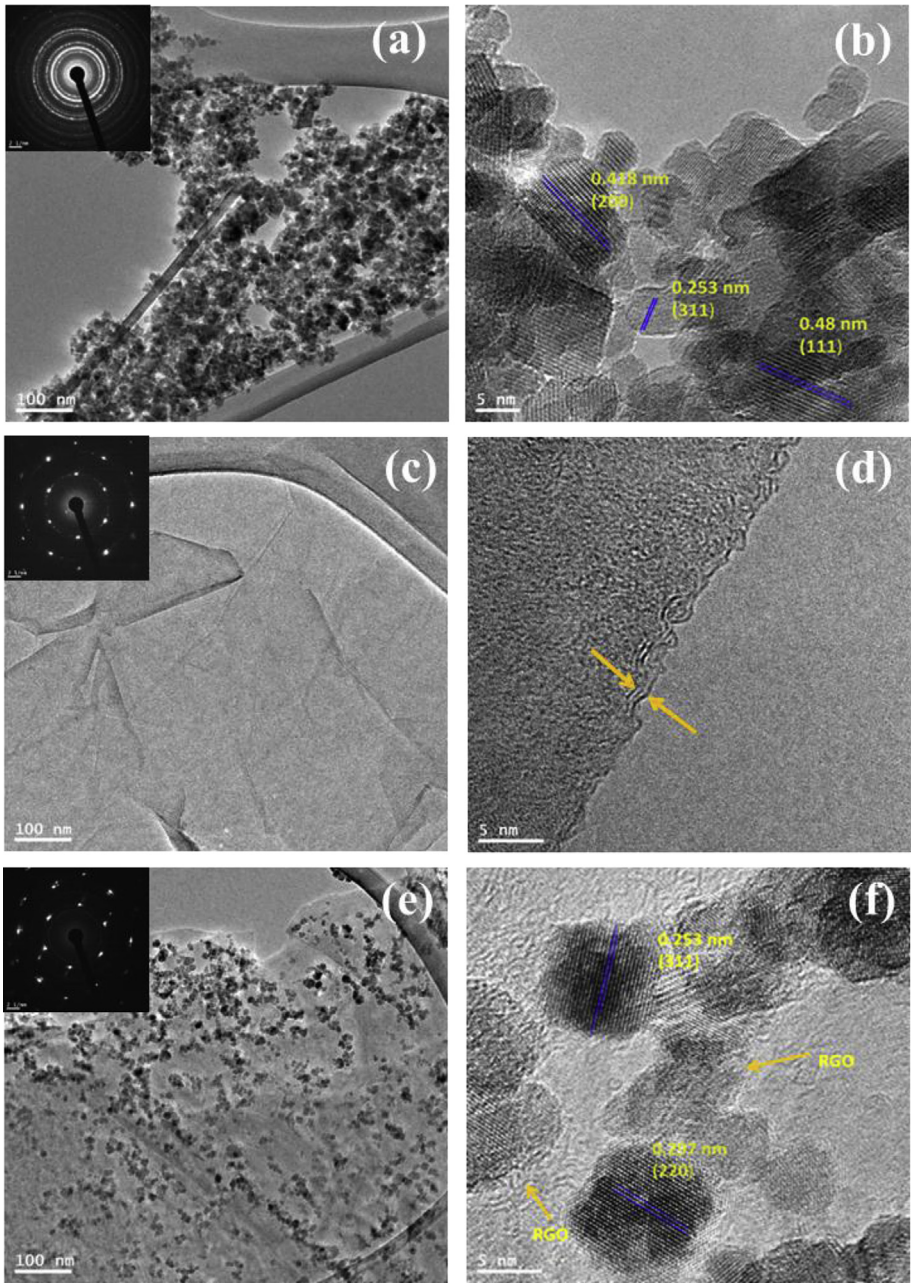

Fig. 7. (a) TEM image (inset shows the SAED pattern), (b) HR-TEM image of the $NiFe_2O_4$ nanoparticles, (c) TEM image (inset shows the SAED pattern), (d) HR-TEM image of RGO, (e) TEM image (inset shows the SAED pattern), and (f) HR-TEM image of the RGO-$NiFe_2O_4$ nanocomposite.

4.7. XPS analysis

The chemical composition and extent of reduction in RGO and the RGO-$NiFe_2O_4$ nanocomposite were analyzed by XPS, as shown in Fig. 8(a–e). The XPS survey scan of RGO confirmed the presence of C 1s and O 1s spectra. The atomic wt. % ratio of C:O was determined to be ~9.25, which is significantly higher than that of GO (2.3) [45]. This result suggests the removal of oxygen-containing functional groups and successful reduction of GO. In the case of the RGO-$NiFe_2O_4$ nanocomposite, peaks corresponding to C 1s, O 1s, Ni 2p, and Fe 2p appeared, indicating the formation of a nanocomposite phase, as shown in Fig. 8(a). The atomic wt. % of C:O was ~1.14 including the oxygen content from the $NiFe_2O_4$ phase. Fig. 8(b and c) shows deconvoluted XPS spectra of the Ni and Fe core electrons. As shown in Fig. 8(b), the Ni 2p spectrum was fitted by a Gaussian–Lorentzian function with two spin–orbit doublets (Ni $2p_{3/2}$ and Ni $2p_{1/2}$), characteristic of Ni^{3+} and Ni^{2+} along with two shakeup satellites (identified as "Sat."). Similarly, the Fe 2p spectrum was fit with two spin–orbit doublets (Fe $2p_{3/2}$ and Fe $2p_{1/2}$), characteristic of Fe^{2+} and Fe^{3+} along with two shakeup satellites, as shown in Fig. 8(c). This analysis further suggests that the $NiFe_2O_4$-RGO nanocomposite contains Ni^{3+}, Ni^{2+}, Fe^{2+}, and Fe^{3+} ionic states [46].

In the case of Ni, the broad peak in the range of 850 eV corresponds to Ni $2p_{3/2}$, whereas the small peak in the range of 860–872 eV corresponds to Ni $2p_{1/2}$, as shown in Fig. 8(b). Further, the broad peak in the range of 710 eV corresponds to Fe $2p_{3/2}$, whereas the small peak in the range of 725 eV corresponds to Fe $2p_{1/2}$, as shown in Fig. 8(c). It is well-known that $NiFe_2O_4$ possesses a cubic crystal structure. In the cubic spinel crystal, Ni^{3+}, Ni^{2+}, Fe^{2+}, and Fe^{3+} cations can be surrounded by six O^{2-} anions in

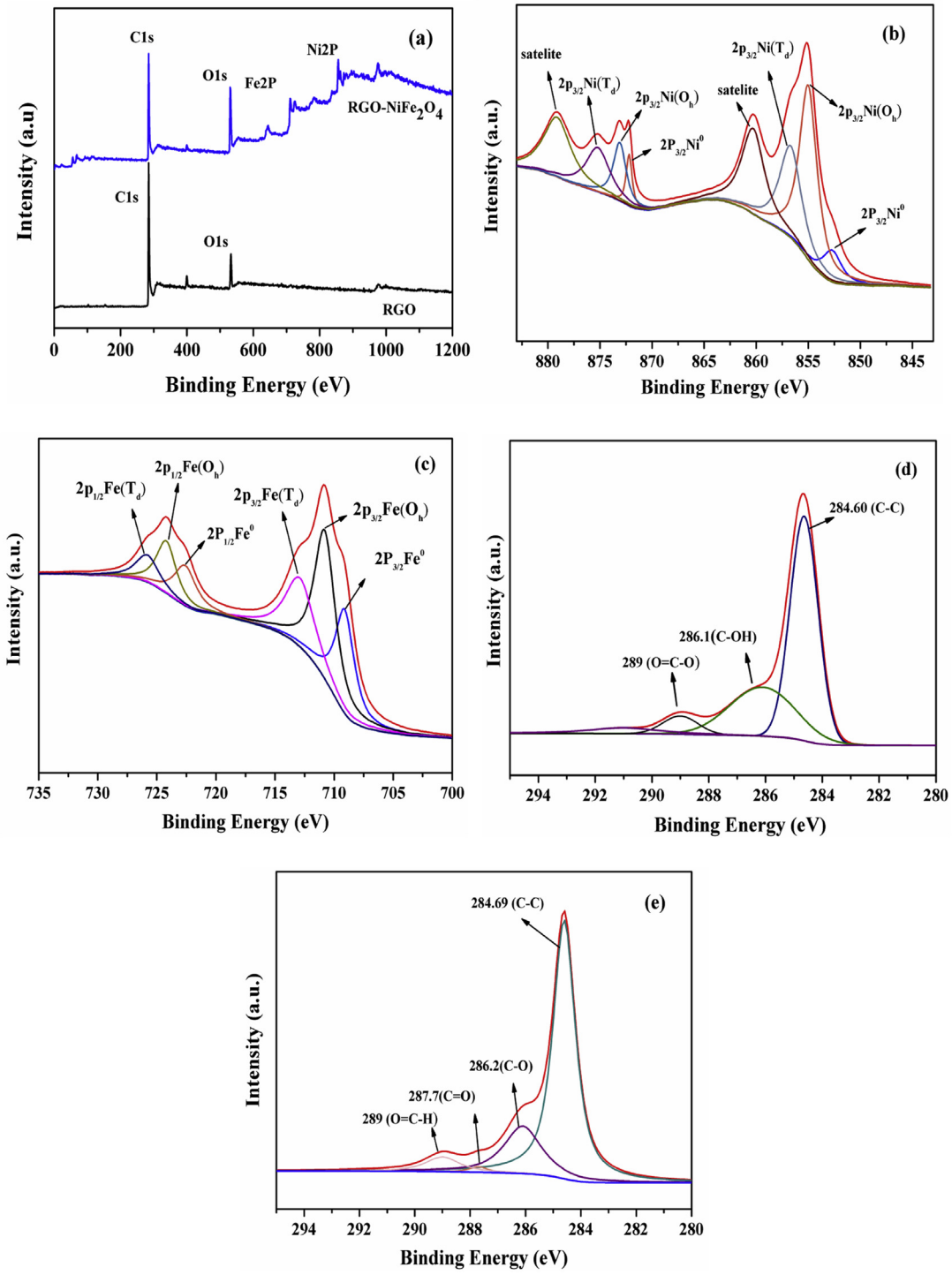

Fig. 8. (a) XPS curves of RGO and the RGO-$NiFe_2O_4$ nanocomposite, and deconvoluted spectra of (b) Ni2p, (c) Fe2p of the RGO-$NiFe_2O_4$ nanocomposite, (d) C1s of RGO, and (e) C1s of RGO-$NiFe_2O_4$ nanocomposite.

octahedral voids whereas four O^{2-} anions are in tetrahedral voids. The deconvoluted C1s spectra of RGO and RGO-$NiFe_2O_4$ shown in Fig. 8(d-e) reveal the peaks corresponding to C—C, C—O, O═C—O, and O═C—OH groups. Moreover, the binding energy corresponding to (C—C) changes in the C 1s spectra of RGO and RGO-$NiFe_2O_4$, suggesting the existence of charge transfer between RGO and the $NiFe_2O_4$ nanoparticles [47].

4.8. Electrochemical studies

4.8.1. Electrochemical characterization of the RGO-$NiFe_2O_4$ electrode

The RGO-$NiFe_2O_4$ composite-modified GCE was characterized by evaluating the effect of the scan rate in a 0.1 M KOH solution. Fig. 9 shows the CVs obtained for the RGO-$NiFe_2O_4$ composite-

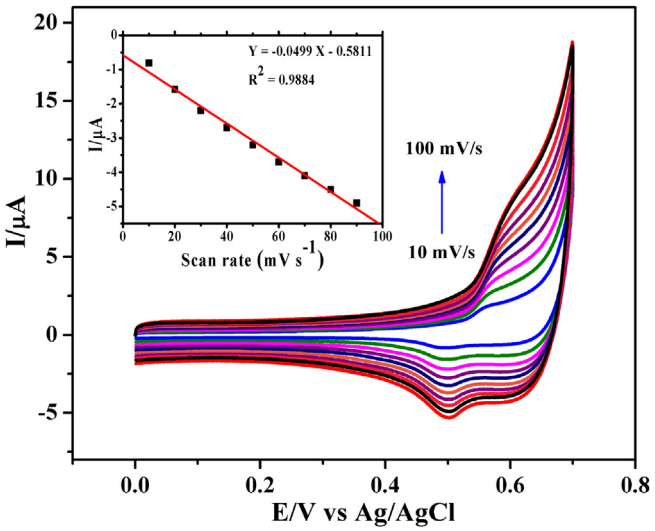

Fig. 9. CV curves for RGO-$NiFe_2O_4$-modified GCE at scan rates of 10, 20, 30, 40, 50, 60, 70, 80, 90, and 100 mV/s in a 0.1 M KOH solution (the inset shows a plot of the scan rate versus current).

modified GCE in a 0.1 M KOH solution at various scan rates (10–100 mV/s). A pair of redox peaks was observed at +0.55 V and +0.5 V, corresponding to the oxidation and reduction of Fe and Ni, respectively. Since the oxidation potentials of these metal ions are close, the oxidations peaks were not separated in the CV. With increasing scan rate from 10 to 100 mV s^{-1}, the cathodic and anodic peak currents increased. The plot of the scan rate versus the anodic peak current was linear with a correlation coefficient of 0.9884 [inset of Fig. 9]. This suggests the surface confined oxidation of the RGO-$NiFe_2O_4$ composite in the 0.1 M KOH solution.

4.8.2. Electrochemical oxidation of hydrazine

The electrochemical catalytic activity of the RGO-$NiFe_2O_4$ composite was analyzed by utilizing hydrazine as a probe. The mechanism for the oxidation of hydrazine can be described as follows.

$$N_2H_4 + 4\,OH^- \rightarrow N_2 + 4H_2O + 4e^-$$

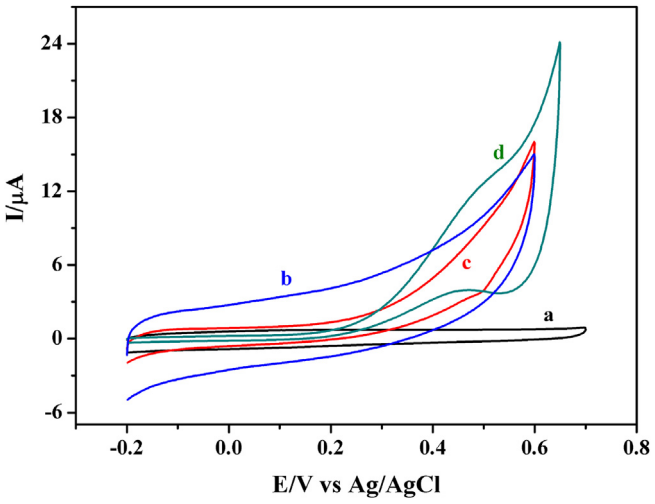

Fig. 10. CV curves for a: bare GCE, b: RGO, c: $NiFe_2O_4$, and d: RGO-$NiFe_2O_4$-modified GCEs for 1 mM hydrazine in a 0.1 M KOH solution at a scan rate of 50 mV/s.

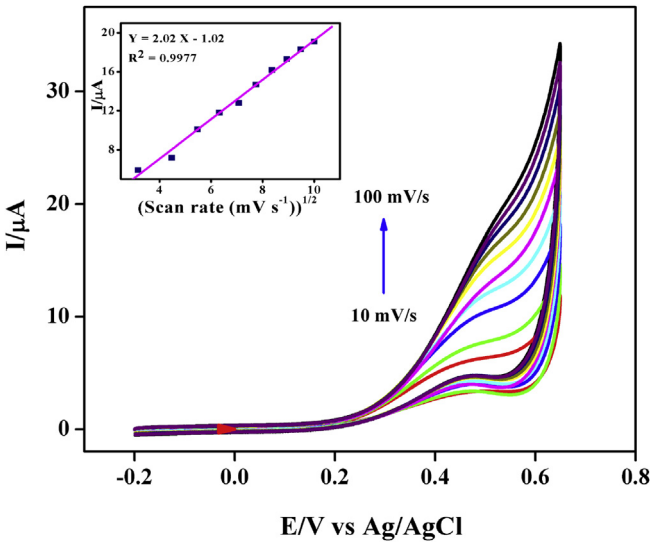

Fig. 11. CV curves for 1 mM hydrazine for the RGO-$NiFe_2O_4$-modified GCE at scan rates of 10, 20, 30, 40, 50, 60, 70, 80, 90, and 100 mV/s in a 0.1 M KOH solution (the inset shows a plot of the square root of the scan rate versus current).

Fig. 10 shows the CVs obtained for 1 mM hydrazine in 0.1 M KOH for the bare GCE, RGO, $NiFe_2O_4$, and RGO-$NiFe_2O_4$-modified GCEs. No significant oxidation peak was observed for the oxidation of hydrazine for the bare GCE in the potential window between −0.2–0.6 V. Although the oxidation peak was not well resolved at the RGO-modified GCE, the background current increased, which may be due to the oxidation of hydrazine. On the other hand, the $NiFe_2O_4$-modified GCE also improved the electrochemical oxidation of hydrazine compared to the bare and RGO-modified GCEs. In the case of the RGO-$NiFe_2O_4$ composite-modified GCE, the oxidation peak current was observed at 0.48 V with an enhanced oxidation current compared to the bare GCE, RGO, and $NiFe_2O_4$-modified GCEs. In the reverse scanning, a cathodic peak was observed which may be due to the reduction of Ni and Fe metal ions. The absence of any other reduction peaks suggests that the oxidation of hydrazine is an irreversible process at the RGO-$NiFe_2O_4$ composite-modified GCE. Due to the synergistic

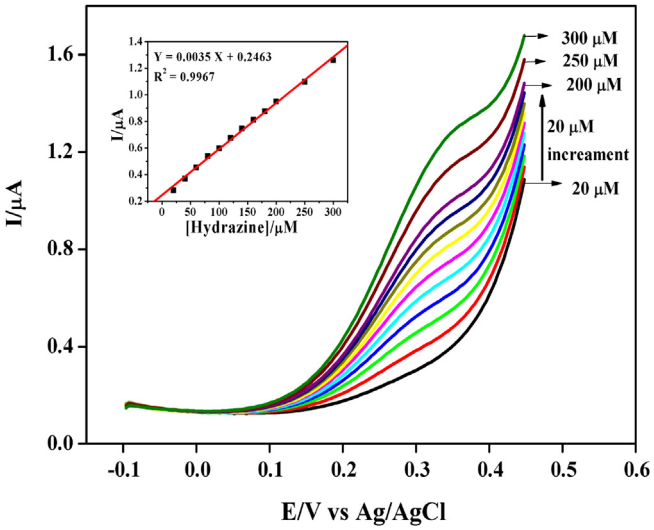

Fig. 12. DPV curves for the RGO-$NiFe_2O_4$-modified GCE with various concentrations of hydrazine in a 0.1 M KOH solution (the inset shows a plot of the concentration of hydrazine versus current).

effect of RGO and $NiFe_2O_4$ towards the oxidation of hydrazine, a higher oxidation current as well as a less positive potential shift was observed for the RGO-$NiFe_2O_4$ composite-modified GCE. Hence, this electrode could be used for the determination of hydrazine. Further, the effect of the scan rate on the oxidation of hydrazine was studied by varying the scan rate from 10 to 100 mV s^{-1} in a 0.1 M KOH solution containing 1 mM hydrazine, as shown in Fig. 11. Upon increasing the scan rate, the oxidation peak current of hydrazine also increased. The plot of the square root of the scan rate versus the oxidation peak current of hydrazine was linear with a correlation coefficient of 0.9977. This confirms that the oxidation of hydrazine was a diffusion controlled process for the RGO-$NiFe_2O_4$ composite-modified GCE. The effect of the concentration on the oxidation of hydrazine was also evaluated by increasing the concentration of hydrazine with the RGO-$NiFe_2O_4$ composite-modified GCE. Fig. 12 shows the DPVs obtained for as the concentration of hydrazine was increased from 20 μM to 300 μM for the RGO-$NiFe_2O_4$ composite-modified GCE. The oxidation peaks of hydrazine uniformly increased in the concentration range and the plot of the oxidation peak current versus the concentration was linear with a correlation coefficient of 0.9996. This confirms that the detection of hydrazine can be carried out using the RGO-$NiFe_2O_4$ composite-modified GCE.

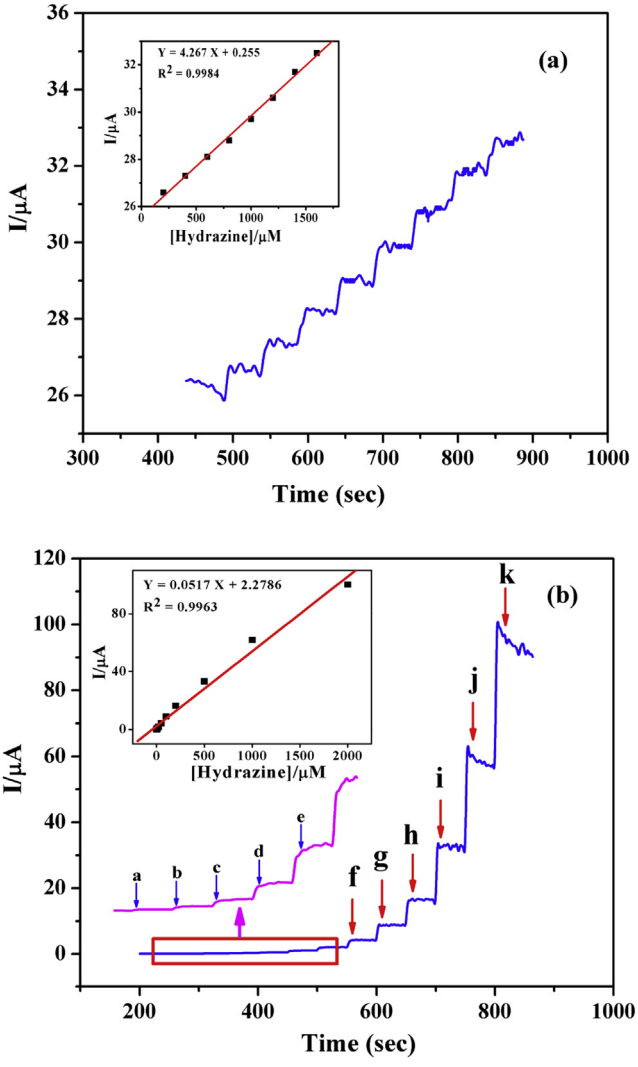

Fig. 13. Amperometric *i–t* curve of RGO-$NiFe_2O_4$-modified GCE for the detection of hydrazine in a 0.1 M KOH solution, where E_{app} = +0.55 V at a time regular interval of 50 s; each step increases the concentration of hydrazine **(a)** by 200 nM and **(b)** by a: 0.2, b: 0.5, c: 1, d: 2, e: 5, f: 10, g: 20, h: 50, i: 100, j: 200, and k: 500 μM (the **insets show** linear relation between the concentration of hydrazine and the oxidation current).

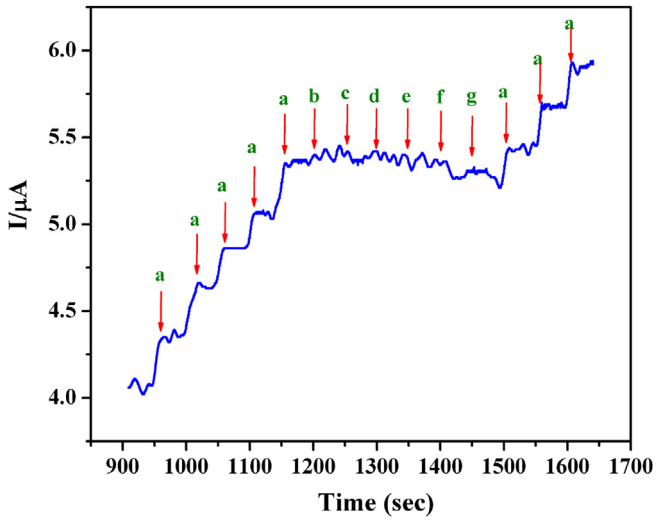

Fig. 14. Amperometric i–t curve of RGO-$NiFe_2O_4$-modified GCE for the detection of a: 500 nM hydrazine in the presence of 100 μM of different interferentes of b: $MgSO_4$, c: $CuSO_4$, d: $CaCl_2$, e: NaF, f: NH_4Cl, and g: oxalic acid in 0.1 M KOH, where E_{app} = +0.55 V.

4.8.3. *Amperometric determination of hydrazine*

Amperometric analysis was used to investigate the sensitivity of the RGO-$NiFe_2O_4$ electrode towards the detection of the electro-oxidation of hydrazine. Fig. 13 shows the amperometric i-t curves of hydrazine for the RGO-$NiFe_2O_4$-modified electrode in a homogeneously stirred 0.1 M KOH solution by applying a constant potential of +0.55 V. The RGO-$NiFe_2O_4$-modified electrode shows an initial current response due to 200 nM hydrazine [Fig. 13(a)]. Further addition of 200 nM hydrazine in each step with a sample interval of 50 s increased the current response of the oxidation of hydrazine. The plot of the concentration of hydrazine versus the oxidation peak current was linear with a correlation coefficient of 0.9984 [inset of Fig. 13(a)]. When the concentration of hydrazine was increased from 0.2 μM to 500 μM, the oxidation of hydrazine also increased and the plot of the concentration versus the peak current was linear with a correlation coefficient of 0.9963 [inset of Fig. 13(b)]. The observed amperometric current response with a higher sensitivity for hydrazine at the RGO-$NiFe_2O_4$ electrode indicates that the modified electrode can be successfully used for the determination of 200 nM hydrazine. Further, the effect of interference on the determination of hydrazine was also evaluated at the RGO-$NiFe_2O_4$-modified GCE. Fig. 14 shows the amperometric i-t curve for hydrazine at the RGO-$NiFe_2O_4$-modified GCE in the presence of several interferences in a homogeneously stirred 0.1 M KOH solution. The increased initial current response was due to the addition of 500 nM hydrazine. After five additions, no changes of the current response were observed with the addition of 100 μM each of Mg^{2+}, Cu^{2+}, Ca^{2+}, Na^{+}, NH_4^{+}, and oxalic acid to the same solution. Subsequently, 500 nM of DOPAC was added to the same 0.1 M KOH solution and an increase of the current response was observed which was similar to the current response observed in the earlier steps. The above results indicate that the detection of 500 nM is possible even in the presence of 200-fold excesses of common interferences.

5. Conclusions

An RGO-$NiFe_2O_4$ nanocomposite was synthesized by a simple *in situ* hydrothermal approach and characterized in detail. TEM studies revealed that $NiFe_2O_4$ nanoparticles were well dispersed on the RGO sheets with an average diameter of ~10 nm. The XPS analysis confirmed the oxidation states of Ni and Fe in RGO-$NiFe_2O_4$ as well as the reduction of GO. Further, the electrochemical oxidation of hydrazine was evaluated for the bare GCE, RGO, $NiFe_2O$, and RGO-$NiFe_2O_4$-modified GCEs. Due to the synergistic effect between RGO and $NiFe_2O_4$, enhanced electrochemical activity was observed for the RGO-$NiFe_2O_4$ nanocomposite-modified GCE compared to the other modified electrodes. Using amperometry, the detection of 200 nM of hydrazine was achieved. To conclude, the facile approach utilized for the synthesis of the nanocomposite and its enhanced catalytic activity make the RGO-$NiFe_2O_4$ nanocomposite a suitable candidate for the electro-oxidation of hydrazine and could be used as a sensor material in the near future.

Acknowledgments

This study was supported by the Basic Research Laboratory Program (2014R1A4A1008140) through the Ministry of Science, ICT & Future Planning. This work was also supported by the Basic Science Research Program through the National Research Foundation (NRF) funded by the Ministry of Education of Korea (2013R1A1A2011608).

References

[1] Raoof JB, Ojani R, Jamali F, Hosseini SR. Electrochemical detection of hydrazine using a copper oxide nanoparticle modified glassy carbon electrode. Casp J Chem 2012;1:73–85.
[2] Aldous L, Compton RG. The mechanism of hydrazine electro-oxidation revealed by platinum microelectrodes: role of residual oxide. Phys Chem Chem Phys 2011;13:5279–87.
[3] Rosca V, Duca M, Groot D, Matheus T, Koper MTM. Nitrogen cycle electrocatalysis. Chem Rev 2009;109:2209–44.
[4] Asazawa K, Yamada K, Tanaka H, Taniguchi M, Oguro K. Electrochemical oxidation of hydrazine and its derivatives on the surface of metal electrodes in alkaline media. J Power Sources 2009;19:362–5.
[5] Granot E, Filanovsky B, Presman I, Kuras I, Patolsky F. Hydrazine/air direct-liquid fuel cell based on nanostructured copper anodes. J Power Sources 2012;204:116–21.
[6] Jannakoudakis AD, Kokkinidis G. Anodic oxidation of hydrazine and its methylderivatives on bare Pt and Pt electrode surfaces modified by underpotential metal adsorbates in acetonitrile. J Electroanal Chem 1982;134:311–24.
[7] Liu J, Zhou W, You T, Li F, Wang E, Dong S. Detection of hydrazine, methylhydrazine, and isoniazid by capillary electrophoresis with a palladium-modified microdisk array electrode. Anal Chem 1996;68:3350–3.
[8] Hosseini MG, Momeni MM, Zeynali S. Au nanoparticle-doped TiO_2 nanotubes catalysts prepared by anodizing and electroplating methods and its application for nitrite detection. J Mat Sci Eng B 2012;2:16–23.
[9] Yi Q, Lei L, Yu W, Zhou Z, Xu G. A novel titanium-supported Ag/Ti electrode for the electro-oxidation of hydrazine. J Mole Catal A-Chem 2008;295:34–8.
[10] Koczkur K, Yi QF, Chen A. Nanoporous Pt-Ru networks and their electrocatalytical properties. Adv Mater 2007;19:2648–52.
[11] Wang J, Dong JZ, Huang J, Li J, Jin X, Niu J, et al. Filling carbon nanotubes with Ni–Fe alloys via methylbenzene-oriented constant current electrodeposition for hydrazine electrocatalysis. Appl Surf Sci 2013;270:128–32.
[12] Yamazaki S, Ioroi T, Tanimoto K, Yasuda K, Asazawa K, Yamaguchi S, et al. Electrochemical oxidation of hydrazine derivatives by carbon-supported metalloporphyrins. J Power Sources 2012;204:79–84.
[13] Koo Y, Littlejohn G, Collins B, Yun Y, Vesselin NS, Schulz M, et al. Synthesis and characterization of Ag-TiO_2-CNT nanoparticle composites with high photocatalytic activity under artificial light. Compos Part B 2014;57:105–11.
[14] Ivanov S, Lange U, Tsakova V, Vladimir MM. Electrocatalytically active nanocomposite from palladium nanoparticles and polyaniline: oxidation of hydrazine. Sens Actuators B Chem 2010;150:271–8.
[15] Sing SK, Iizuka Y, Xu Q. Nickel-palladium nanoparticle catalyzed hydrogen generation from hydrous hydrazine for chemical hydrogen storage. Int J Hydrogen Energ 2011;36:11794–2801.
[16] Yanagimoto K, Majima K, Sunada S, Sawada T. Effects of surface modification on surface structure and electrochemical properties of Mm(Ni,Co,Mn,Al) alloy powder. J Alloy Compd 2004;377:174–8.
[17] Srivastava M, Das AK, Khanra P, Uddin ME, Kim NH, Lee JH. Characterizations of in situ grown ceria nanoparticles on reduced graphene oxide as a catalyst for the electrooxidation of hydrazine. J Mater Chem A 2013;1:9792–801.
[18] Srivastava M, Singh J, Kuila T, Layek RK, Kim NH, Lee JH. Recent advances in graphene and its metal-oxide hybrid nanostructured for lithium-ion batteries. Nanoscale 2015;7:4820–68.
[19] Son DI, Yang HY, Kim TW, Park W. Transparent and flexible ultraviolet photodetectors based on ZnO quantum dot/graphene nanocomposites formed on poly(ethylene terephthalate) substrates. Compos Part B 2011;69:154–8.
[20] Tang Q, Chen M, Wang L, Wang G. A novel asymmetric supercapacitors based on binder-free carbon fiber paper at nickel cobaltite nanowires and graphene foam electrodes. J Power Sources 2015;273:654–62.
[21] Li Q, Kim NH, Yoo GH, Lee JH. Positive temperature coefficient characteristic and structure of graphite nanofibers reinforced high density polyethylene/carbon black nanocomposites. Compos Part B 2009;40:218–24.
[22] Zhou G, Wang DW, Yin LC, Li N, Li F, Cheng HM. Oxygen bridges between NiO nanosheets and graphene for improvement of lithium storage. Acs Nano 2012;6:3214–23.
[23] Kuila T, Bose S, Hong CE, Uddin ME, Khanra P, Kim NH, et al. Preparation of functionalized graphene/linear low density polyethylene composites by a solution mixing method. Carbon 2011;49:1033–7.
[24] Srivastava M, Layek S, Singh J, Das AK, Verma HC, Ojha AK, et al. Synthesis, magnetic and Mössbauer spectroscopic studies of Cr doped lithium ferrite nanoparticles. J Alloy Compd 2014;591:174–80.
[25] Carta D, Casula MF, Falqui A, Loche D, Mountjoy G, Sangregorio C, et al. A structural and magnetic investigation of the inversion degree in ferrite nanocrystals MFe_2O_4(M = Mn, Co, Ni). J Phys Chem C 2009;113:8606–15.
[26] He YX, Li Q, Kuila T, Kim NH, Jiang T, Lau KT, et al. Micro-crack behavior of carbon fiber reinforced thermoplastic modified epoxy composites for cryogenic applications. Compos Part B 2013;44:533–9.
[27] Grinou A, Yun YS, Cho SY, Park HH, Jin HJ. Dispersion of Pt nanoparticle-doped reduced graphene oxide using aniline as a stabilizer. Mater Sci 2012;5:2927–36.
[28] Hummers W, Offeman R. Preparation of graphitic oxide. J Am Chem Soc 1958;80. 1339–9.
[29] Kuila T, Mishra AK, Khanra P, Kim NH, Lee JH. Recent advances in the efficient reduction of graphene oxide and its application as energy storage electrode materials. Nanoscale 2013;5:52–71.
[30] Park OK, Kim NH, Yoo GH, Rhee KY, Lee JH. Effects of the surface treatment on the properties of polyaniline coated carbon nanotubes/epoxy composites. Compos Part B 2010;41:2–7.
[31] Ding R, Qi L, Jia M, Wang H. Sodium dodecyl sulfate-assisted hydrothermal synthesis of mesoporous nickel cobaltite nanoparticles with enhanced catalytic activity for methanol electrooxidation. J Power Sources 2014;251:287–95.
[32] Du FP, Wang JJ, Tang CY, Tsui CP, Xie XL, Yung KF. Enhanced electrochemical capacitance of polyaniline/graphene hybrid nanosheets with graphene as templates. Compos Part B 2013;53:376–81.
[33] Bose S, Kuila T, Uddin ME, Kim NH, Lau AKT, Lee JH. In-situ synthesis and characterization of electrically conductive polypyrrole/graphene nanocomposites. Polymer 2010;51:5921–8.
[34] Ren L, Qiu J, Wang S. Photovoltaic properties of graphene nanodisk-integrated polymer composites. Compos Part B 2013;55:548–57.
[35] Kim NH, Khanra P, Kuila T, Jung D, Lee JH. Efficient reduction of graphene oxide using Tin-powder and its electrochemical performances for use as an energy storage electrode material. J Mater Chem A 2013;1:11320–8.
[36] Li P, Kim NH, Heo SB, Lee JH. Novel PAAm/Laponite clay nanocomposite hydrogels with improved cationic dye adsorption behavior. Compos Part B 2008;39:756–63.
[37] Hu L, Wu L, Liao M, Hu X, Fang X. Electrical transport properties of large, individual $NiCo_2O_4$ nanoplates. Adv Funct Mater 2012;22:998–1004.
[38] Johannes PM, Ansurat W, Phokharatkul D, Lomas TA, Tusntranont A. Novel surfactant-stabilized graphene-polyaniline composite nanofiber for supercapacitor applications. Compos Part B 2015;77:93–9.
[39] Zhang H, Kuila T, Kim NH, Yu DS, Lee JH. Simultaneous reduction, exfoliation, and nitrogen doping of graphene oxide via a hydrothermal reaction for energy storage electrode materials. Carbon 2014;69:66–78.
[40] Sivakumar P, Ramesh R, Ramanand A, Ponnusamy S, Muthamizhchelvan C. Preparation and properties of nickel ferrite ($NiFe_2O_4$) nanoparticles via sol-gel auto-combustion method. Mater Res Bull 2011;46:2204–7.
[41] Bhadra S, Kim NH, Lee JH. Synthesis of water soluble sulfonated polyaniline and determination of crystal structure. J Appl Polym Sci 2010;117:2025–35.
[42] Tuinstra F, Koenig JL. Raman spectrum of graphite. J Chem Phys 1970;53:1126–30.

[43] Uddin ME, Kuila T, Nayak GC, Kim NH, Ku BC, Lee JH. Effects of various surfactants on the dispersion stability and electrical conductivity of surface modified graphene. J Alloy Compd 2013;562:134–42.
[44] Kuilla T, Bhadra S, Yao D, Kim NH, Bose S, Lee JH. Recent advances in graphene based polymer composites. Prog Polym Sci 2010;35:1350–75.
[45] Khan P, Uddin ME, Kim NH, Kuila T, Lee SH, Lee JH. Electrochemical performance of reduced graphene oxide surface-modified with 9-anthracene carboxylic acid. RSC Adv 2015;5:6443–51.
[46] Li L, Wang S, Hui D, Qiu J. Ordered multiphase polymer nanocomposite for high −performance solid-state supercapacitors. Composite Part B 2015;71:40–4.
[47] Joung D, Singh V, Park S, Schulte A, Seal S, Khondake SI. Anchoring ceria nanoparticles on reduced graphene oxide and their electronic transport properties. J Phys Chem C 2011;115:24494–500.